Chapter 4

Brilliance Improvement of a Laser-Produced Soft X-Ray Plasma

Tobias Mey

Additional information is available at the end of the chapter

http://dx.doi.org/10.5772/64149

Abstract

The brilliance of a laser-produced soft X-ray source is enhanced for gaseous target concepts. In contrast to solid or liquid target materials, these sources are clean and versatile but provide a comparably low conversion efficiency of laser energy into EUV and soft X-ray radiation. The basic idea is to induce supersonic effects in the gas jet, leading to a local increase of the particle density, and thus, to a larger number of possible emitters. Typically, the target gas is expanded into a vacuum environment and the density rapidly drops in all directions. In the present approach, a low pressure helium atmosphere is used to generate shock waves in the supersonic nozzle flow. Passing through these structures, the target gas is recompressed, and the particle density is raised. By focusing the laser beam into such regions, a higher number of gas atoms can be ionized resulting in a brighter and smaller plasma.

Keywords: soft X-ray, laser-produced plasma, supersonic jet, barrel shock

1. Introduction

Photons of the soft X-ray spectral region (≈ 0.1–10 nm) have very small absorption lengths in all kinds of material due to the strong interaction with matter [1]. This fact together with the short wavelength qualifies this radiation as a tool for structuring and the analysis with nanometer resolution. An important application is the next-generation lithography that further reduces the achievable feature size in computer chip production [2, 3]. Surface analysis becomes extremely precise by means of reflectometry and scatterometry [4–6] and also the binding state of molecules can be studied by spectral investigations [7–9]. Microscopy with radiation at wavelengths in the water window (λ = 2.3–4.4 nm) allows highly resolved direct

imaging of samples in aqueous environments [10–12]. Mostly, these applications are realized at large-scale facilities, such as synchrotron sources or free-electron lasers. However, the demand for beam time is always too large to be satisfied by these institutions, and thus, people endeavor to transfer experiments to their laboratories. This constitutes the need of compact beam sources as can be realized by the principle of laser-produced plasmas (LPP) that is the subject of this chapter.

In order to classify and compare the radiation of different soft X-ray beam sources, the brilliance *Br* is a commonly used quantity that is the number of photons within a narrow spectral range $\Delta\lambda/\lambda$ emitted into a solid angle Ω from an area A within the time scale τ (typically the wavelength range $\Delta\lambda$ is defined to be 0.1% of the central wavelength λ) [1]:

$$Br = \frac{N_{ph}}{\tau \cdot A \cdot \Omega \cdot \Delta\lambda / \lambda}. \tag{1}$$

The value of *Br* is given in the unit $1/(s{\cdot}mm^2{\cdot}mrad^2 \cdot 0.1\%BW)$ with 0.1%BW indicating the bandwidth of 0.1%. A distinction is made between the peak brilliance, where τ denotes the pulse duration, and the average brilliance, where τ is the inverse of the repetition rate.

In comparison to synchrotrons and free-electron lasers, the brilliance of laser-produced plasma sources is several orders of magnitude lower. However, there are strategies to increase their brilliance which involve, e.g., higher power densities of the generating laser pulse. On the other hand, the density of the target material has a strong impact on the achievable number of soft X-ray photons too, whereas basically the source brilliance scales with the density. Thus, the brightest plasmas can be achieved with solids. Respective target materials are deposited on rotating cylinders [13] or quickly moving tapes [14], which provide repetition rates of up to 1 kHz. Prominent elements are gold or tin for the production of radiation at a wavelength of 13.5 nm, which is applied in EUV lithography [15]. Furthermore, there are sources employing cold gases in a solid phase, such as an argon filament that emits soft X-rays in the wavelength range 2–5 nm [16]. Achievable plasma sizes with solid targets are comparably small and on the order of several tens of μm (full-widths at half-maximum, FWHM).

A plasma of similar brilliance and extent is obtained with liquid targets, e.g., xenon [17], methanol [18], or tin [15]. A fluid jet [19] provides high target densities but might lead to size and brightness fluctuations. Going one step further to individual microscopic droplets [20], the advantage is the mass limitation such that the entire target material is converted into a highly ionized plasma state, supporting source stability. However, the drawback of solid and liquid target concepts is the inevitable production of fast particles and ions with kinetic energies of up to several hundred keV [21], which severely damage optics in the beam path. There are mitigation strategies to slow down the debris material such as repeller fields [22] or localized gas jet shields [23], but still the collector optics has a limited lifetime [2]. Contrarily, gaseous targets are almost free from debris [24]. Short gas pulses with durations of μs to ms are expanded from a pressure of several 10 bar into vacuum by a piezomechanical or electromagnetic nozzle, resulting in a supersonic jet. Different target gases feature individual spectra

http://dx.doi.org/10.5772/64149

of the resulting radiation, ranging from emitters with characteristic spectral lines (low atomic number, e.g., nitrogen) to broadband emitters (high atomic number, e.g., xenon) [25]. However, here, the conversion efficiency from laser energy into soft X-ray energy is comparably low due to the low density of the target material. Furthermore, achievable plasma sizes of several 100 μm are large. For metrology or scientific applications, though, these sources are very attractive due to their high cleanliness and versatility [8, 26].

In this study, a brilliance enhancement of laser-produced plasmas is demonstrated for gaseous jet targets, making use of supersonic effects. First, the theoretical background is provided to describe the physical properties of laser-produced plasmas as well as the gas dynamics of the related jet target. Experimental techniques are introduced that are employed to characterize the plasma and the gas jet. The effect of supersonic shocks within the target gas is investigated in both ways, theoretically and experimentally, revealing a significant brilliance enhancement for plasmas generated in respective shock regions. This chapter is based on a previous publication by Mey et al. [25] and has been revised and extended partly.

2. Physical properties of a plasma

Initially, the laser beam that irradiates the target material creates ions by multiphoton absorption, tunneling, or field ionization [27]. The resulting free electrons are accelerated by the strong electric field leading to inverse bremsstrahlung and avalanche ionization. A hot dense plasma state is generated. In competition to the heating processes, deionization takes place in terms of diffusion and recombination [27]. Depending on the electron temperature, a continuum of electromagnetic radiation is produced due to bremsstrahlung and recombination of free electrons with ions. Additionally, bound–bound transitions within the ions contribute narrow lines to the emission spectrum. A corresponding scheme is depicted in **Figure 1**.

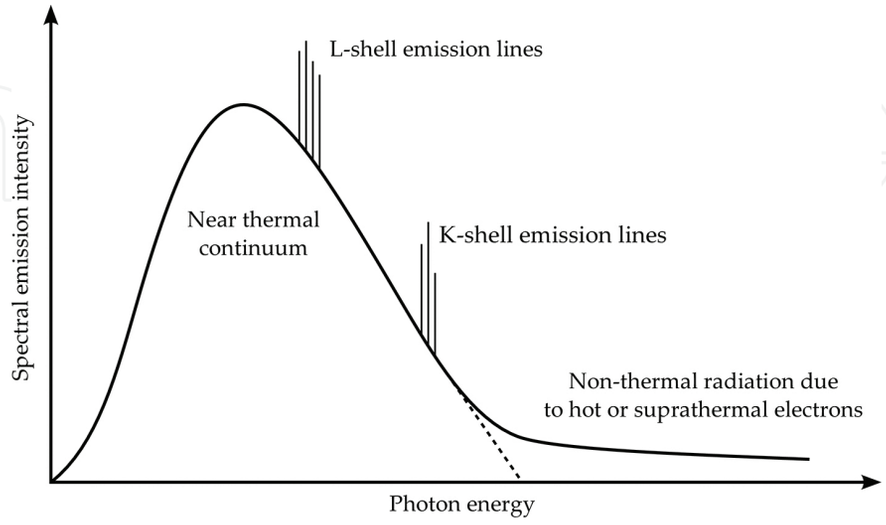

Figure 1. Scheme of the emission spectrum of a hot dense plasma.

The thermodynamics within a hot dense plasma can be approximated by the idealized state of a thermal plasma that is characterized by a single electron temperature T and a corresponding Maxwell velocity distribution. Within that simplification, the plasma may be treated as a blackbody that emits radiation with a continuous spectrum. The assumption that photons are emitted carrying discrete quanta of energy, with energy proportional to frequency, leads to the spectral energy density [1]

$$Br = 3.146 \times 10^{11} \left(\frac{k_B T}{\mathrm{eV}} \right)^3 \frac{\left(\frac{\hbar\omega}{k_B T} \right)^3}{e^{\frac{\hbar\omega}{k_B T}} - 1} \frac{Photons}{mm^2\, mrad^2 s\ (0.1\%BW)} \tag{2}$$

here, given in units of the brilliance with Planck's constant $\hbar$ and the photon frequency ω. Typical electron temperatures for gas targets irradiated by nanosecond laser pulses are 20–200 eV [28, 29]. The corresponding spectral maxima of the Planck distribution are found at the photon wavelengths 2.2–22.0 nm with peak brilliances of 3.6 × 10^{15} to 3.6 × 10^{18} 1/(s mm^2 mrad^2). In fact, a laser-produced plasma is far away from thermodynamic equilibrium and a thermal plasma rather is an upper limit for the spectral power density. However, mostly a two-temperature model is already sufficient to adequately describe the continuum radiation by a hot dense plasma, which is then called near-thermal plasma [1]. In addition to the thermal electrons, a suprathermal component is introduced which is raised by nonlinear interactions such as resonant absorption. When these electrons undergo bremsstrahlung or recombination, they give rise to a high photon energy tail in the emission spectrum as indicated in **Figure 1**. Line radiation is emitted when electrons change their energy state within an ion from an outer to an inner electron shell. The resulting photon energy corresponds to the transition energy of the electron as described by Moseley's law, which is an extension of the Rydberg formula [30]

$$\frac{1}{\lambda} = \frac{R_\infty}{1 + m_e / m_{nuc}} \left(Z_{at} - S_{sh} \right)^2 \left(\frac{1}{n_1^2} - \frac{1}{n_2^2} \right) \tag{3}$$

with the Rydberg constant R_∞, the nuclear mass m_{nuc}, and the atomic number Z_{at}. The constant S_{sh} describes the shielding due to electrons between the core and the considered electron. Furthermore, n_1 and n_2 are the principal quantum numbers of the initial and final states of the electron. In plasmas of species with low atomic numbers like nitrogen ($Z_{\mathrm{at}} = 7$), comparatively few free electrons are produced and the emitted radiation is dominated by single spectral lines. In contrast, elements with high atomic numbers such as xenon ($Z_{\mathrm{at}} = 54$) yield much more free electrons, resulting in a spectrum of numerous closely packed lines and a significant thermal contribution.

Another important plasma parameter is the electron plasma frequency [1]

http://dx.doi.org/10.5772/64149

$$\omega_p = \left(\frac{e^2 n_e}{\epsilon_0 m_e} \right)^{1/2} \tag{4}$$

at which the free electrons tend to oscillate (where e is the electron charge, n_e is the electron density, m_e is the electron mass, and ϵ_0 is the vacuum permittivity). As a consequence, an incident electromagnetic wave can propagate in the plasma only if its frequency ω is greater than ω_p and it is totally reflected if $\omega = \omega_p$. This yields a critical electron density [1]

$$n_c = \frac{\epsilon_0 m_e \omega^2}{e^2} \tag{5}$$

which is $n_c = 1 \times 10^{23}$ cm^{-3} for a common Nd:YAG laser beam with a wavelength of 1064 nm. Thus, when the plasma reaches the critical electron density, it cannot further be heated to pose a limit especially on solid and liquid target concepts. In order to mitigate that limitation, a less intense prepulse can be used to heat the target material and decrease its density precedent to the main pulse [31].

3. Gas dynamics of jet targets

Supersonic gas jets employed as targets inherently exhibit strong density gradients. Here, the basics of supersonic nozzle flows and related shock phenomena are described theoretically, mainly based on [32, 33]. As a result, density estimations of the target gas are provided corresponding to the experimental situation at a laser plasma source.

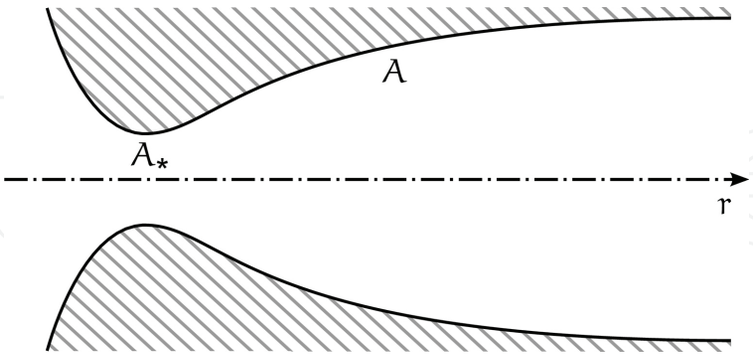

Figure 2. Sketch of a de Laval nozzle. A denotes the local cross-sectional area with the minimum value A_* at its throat position.

Let us first consider the example of a compressible fluid that expands through a convergent-divergent nozzle, a so-called de Laval nozzle as shown schematically in **Figure 2**. In gas dynamics, the basic equations to describe that problem are the conservation laws of mass and energy, formulated for compressible and isentropic flows. It can be shown that these relations

lead to the well-known area relation between the local cross-sectional area A, the throat area A_*, and the local Mach number M [33]

$$\frac{A}{A_*} = \frac{1}{M}\left[\frac{2}{\kappa+1}\left(1+\frac{\kappa-1}{2}M^2\right)\right]^{\frac{\kappa+1}{2(\kappa-1)}}. \tag{6}$$

Here, $\kappa = c_p/c_v$ is the ratio of specific heats (c_p at constant pressure and c_v at constant volume) and the Mach number M is defined as the ratio between the local flow velocity and the local speed of sound. In the present example of a convergent-divergent nozzle, a gas is accelerated in the convergent part according to the continuity equation. If the critical Mach number $M_* = 1$ is reached at the throat, this results in supersonic velocities $M > 1$ in the divergent part, and the thermal energy of the gas is efficiently converted into directed kinetic energy. Concurrently, the gas density decreases according to the relation [32]

$$\frac{\rho}{\rho_0} = \left(1+\frac{\kappa-1}{2}M^2\right)^{-\frac{1}{\kappa-1}} \tag{7}$$

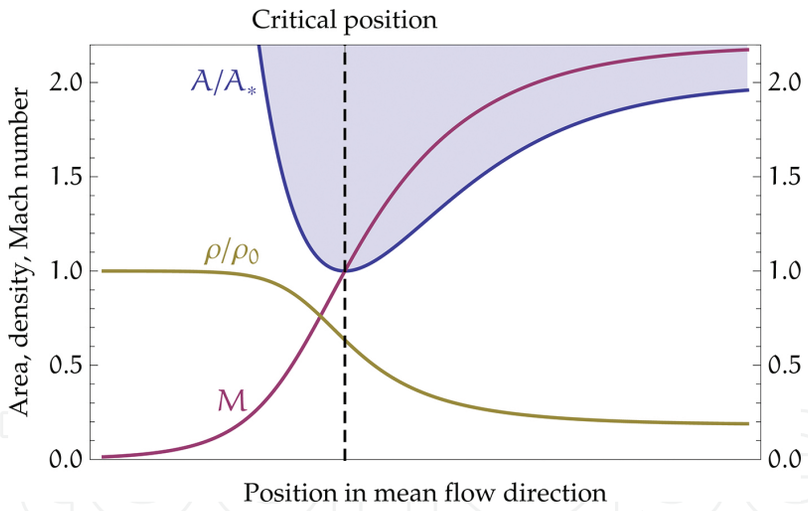

Figure 3. State functions of a flow in a de Laval nozzle: density ρ in terms of its stagnation value ρ_0, Mach number M and the local cross-sectional area A reaching A_* at its throat position. A diatomic gas with $\kappa = 7/5$ is assumed.

The shape of the cross-sectional area A/A_* of a typical de Laval nozzle is shown in **Figure 3** together with the resulting distribution of density ρ/ρ_0 (ρ_0 stagnation density) and Mach number M under the assumption of a diatomic gas with $\kappa = 7/5$. Utilizing a supersonic gas jet as a target for laser-produced plasmas requires large particle densities for high conversions efficiencies of laser energy into soft X-ray energy. Thus, a compromise needs to be found between a directed, but rarefied flow at high Mach numbers and divergent but denser flow at low Mach numbers. This can be achieved by adapting the nozzle geometry [34].

http://dx.doi.org/10.5772/64149

Within this work, shock waves, as they can be observed in supersonic flows, are employed to further optimize the particle density in a jet target. Within very short distances on the order of the mean-free path of the molecules, this phenomenon leads to an increase in density, pressure, and temperature while the Mach number decreases. Based on the conservation laws of mass, momentum, and energy, it is possible to derive equations that relate the initial values of those properties with the conditions right behind a shock wave. Here, it is sufficient to consider the change of the initial density ρ and the Mach number M in the case of a normal shock relative to the flow direction. After passing through the shock structure, these properties are denoted as $\hat{\rho}$ and $\hat{M}$, as indicated in **Figure 4**. The corresponding shock relations read [32]

$$\frac{\hat{\rho}}{\rho} = \frac{(\kappa+1)M^2}{2+(\kappa-1)M^2} \tag{8}$$

$$\hat{M} = 1 - \frac{M^2-1}{1+\frac{2\kappa}{\kappa+1}(M^2-1)}. \tag{9}$$

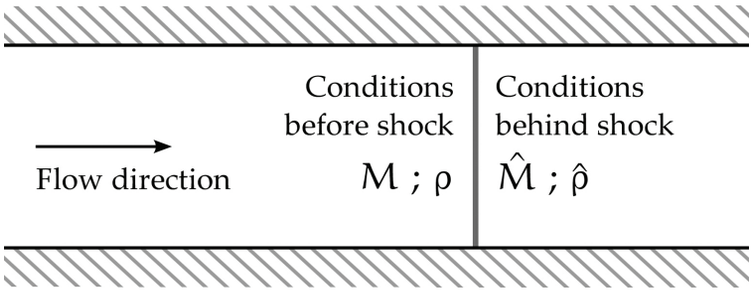

Figure 4. Normal shock structure in a supersonic flow. Gas passing through the shock experiences a decrease from the initial Mach number M to $\hat{M}$ and an increase in density from ρ to $\hat{\rho}$.

Basically, high Mach numbers lead to a strong compression of the fluid when passing through a shock. However, relation (8) defines an upper limit for the density ratio that can be achieved in connection with a shock wave. This limit is approached if $M \to \infty$, and for diatomic gases it is $\frac{\hat{\rho}}{\rho} \to 6$ ($\kappa = 7/5$). At the same time, the Mach number behind the shock decreases to $\hat{M} \to 1/7$. Shock waves appear, e.g., when obstacles perturb a supersonic flow or vice versa, or when objects travel with Mach numbers $M > 1$ through a gas at rest. In the case of a supersonic jet that expands from a stagnation pressure p_0 into an atmosphere with a sufficiently large background pressure p_b, shock waves can also be observed. At a certain distance to the nozzle exit, the collision between the jet particles and the surrounding gas particles leads to a shock structure, which is called barrel shock (see **Figure 5**). With respect to that situation, Muntz et al. introduced the rarefaction parameter [35]

$$\zeta = d_* \frac{\sqrt{p_0 \cdot p_b}}{T_0} \tag{10}$$

where d_* is the throat diameter of the nozzle and T_0 denotes the stagnation temperature. This parameter describes the interaction between jet and background particles, i.e., how strong the expansion flow is influenced by the surrounding gas. Muntz et al. propose a differentiation of the occurring flow into three regimes [35]:

- Scattering regime $\zeta \leq \zeta_s$

  Molecules of the background gas interact with the freely expanding jet by diffusion only, no distinct shock waves evolve.

- Transition regime $\zeta_s < \zeta < \zeta_c$

  Thick lateral shock waves develop and confine an undisturbed core of the jet that is surrounded by a mixing zone of jet and background particles.

- Continuum regime $\zeta_c \leq \zeta$

  The fully evolved barrel shock structure is present, as shown in **Figure 5**. The inner barrel shock waves and the Mach disk spatially delimit the influence of the background gas.

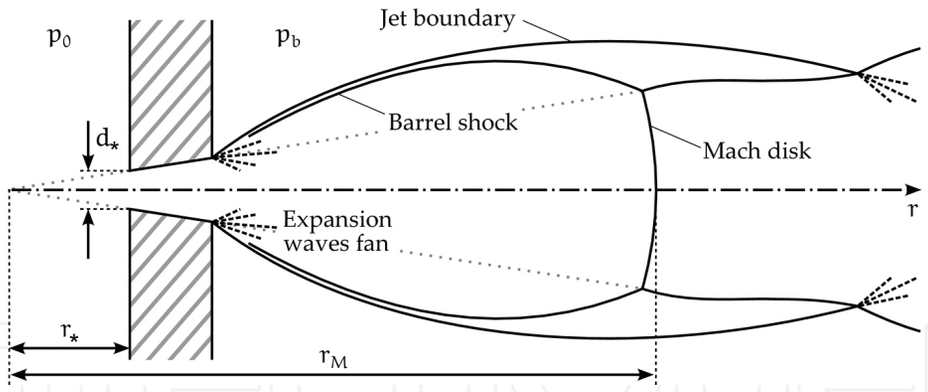

Figure 5. Typical structure of a barrel shock as apparent at supersonic jets in the presence of a background gas. Here, a fluid is expanded from a high pressure p_0 through the conically diverging nozzle into an ambient atmosphere of relatively low pressure p_b. The depicted shock system represents the continuum regime. Adapted from [36].

In the continuum regime, the extent of the shock structure scales with the nozzle pressure ratio p_0/p_b. In particular, within the range $15 < p_0/p_b < 17{,}000$, the distance $l_M = r_M - r_*$ between the nozzle throat and the Mach disk is given by [37]

$$l_M = 0.67 \cdot d_e \sqrt{\frac{p_0}{p_b}} \tag{11}$$

http://dx.doi.org/10.5772/64149

where d_e is the exit diameter of the orifice. It should be noted that this relation has been derived for nozzles with a constant diameter, i.e., for a nondivergent geometry.

In the following, estimations are made for a gas jet with barrel shock structures as it is under experimental investigation in this work too. Nitrogen expands from a pressure of $p_0 = 11$ bar into a helium atmosphere with a pressure of $p_b = 170$ mbar through a conically diverging nozzle (thickness $l_n = 1$ mm, throat diameter $d_* = 300$ μm, and exit diameter $d_e = 500$ μm). At rest, both gases are at room temperature $T_0 = 293$ K. In a simplification, a source flow is assumed corresponding to the dotted cone in **Figure 5** with its apex in a distance of $r_* = 1.5$ mm to the nozzle's throat. According to Eq. (11), the Mach disk appears 2.7 mm behind the nozzle throat, i.e., $r_M = 2.7$ mm. The dimensionless area of the assumed source flow is expressed in terms of the distance r to the virtual source as $A/A_* = (r/r_*)^2$. Solving Eqs. (6) and (7) results in the state functions ρ/ρ_0 and M along the symmetry axis of the nozzle from throat position to the Mach disk, i.e., in the range 1.5 mm < r < 4.2 mm. The conditions directly behind the Mach disk are determined by the shock relations (8) and (9). For r > 4.2 mm, the flow is assumed to be incompressible (ρ = const.) since the Mach number has decreased sufficiently below $M = 1$. Thus, subsequent behavior of M is approximated by the continuity equation $M(r) = \widehat{M} \cdot (r / r_M)^2$.

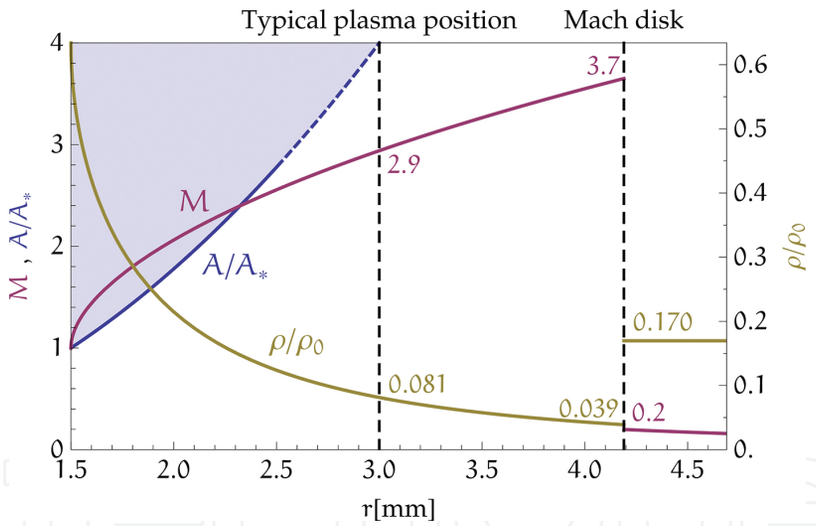

Figure 6. State functions along the symmetry axis of a barrel shock: density ρ in terms of its stagnation value ρ_0, and Mach number M. The solid blue line for A/A_* represents the cross-sectional area of the orifice, whereas the dashed blue line indicates the subsequent conical source flow.

The corresponding state functions $\rho(r)/\rho_0$ and $M(r)$ are depicted in **Figure 6** with respect to the distance r to the virtual source. Usually, the nozzle is operated with a background pressure on the order of $p_b \leq 10^{-4}$ mbar and the plasma is generated in a distance of 500 μm to the nozzle exit. The conditions at the usual plasma position, before and behind the Mach disk, are given in the diagram. It is revealed that due to the shock a two times higher density is achieved in a larger distance to the nozzle as compared to the typical plasma position. In practice, the density increase is even higher since plasma production takes place a few 100 μm besides the symmetry

axis of the nozzle. Here, without ambient gas the jet is even more rarefied and with ambient gas the shock structure is present.

4. The laser-produced soft X-ray source

The setup of a standard soft X-ray source based on gas targets is used [8]. It basically consists of a piezoelectrically operated Proch–Trickl gas valve [38] mounted on a vacuum chamber, and a driving Nd:YAG laser that emits radiation at the fundamental wavelength of 1064 nm with a pulse energy of 800 mJ and a pulse duration of 6 ns (InnoLas SpitLight 600), see **Figure 7**. The intensity profile of the unfocused laser beam, measured by a CCD camera (Lumenera Lu160M), reveals a beam diameter of 5.9 mm (determined through $1/e^2$ decay), corresponding to a mean power density of 4.9×10^8 W/cm^2. Plasma production takes place as soon as a critical power density of $\approx 10^{12}$ W/cm^2 is reached in the focused beam at a sufficiently large particle density [39]. This initiates the first ionization of the target gas followed by avalanche ionization, creating large numbers of free electrons.

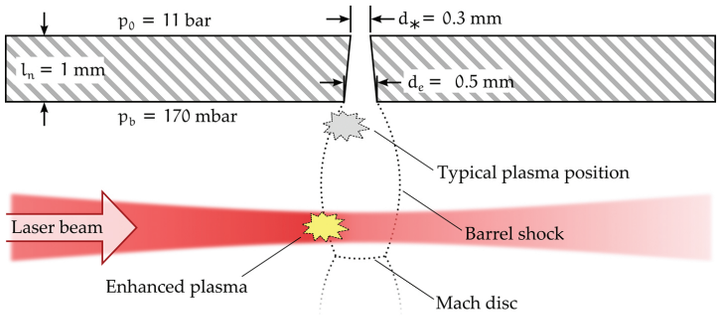

Figure 7. Pinhole camera images of the plasma at a stagnation pressure of $p_0 = 11$ bar for various background pressures p_b as given below the individual figure. The average of 30 single shots is shown.

The target gas is expanded through a divergent nozzle of conical shape. Over a length of l_n = 1 mm, its diameter increases from the throat diameter $d_* = 0.3$ mm to the exit diameter $d_e = 0.5$ mm. The nozzle is opened for a period of 1 ms, generating an underexpanded supersonic jet that expands from stagnation pressure $p_0 = 11$ bar into vacuum, i.e., the background pressure p_b is as low as 10^{-4} mbar. The laser is focused into the gas as soon as the jet flow is steady. The position where the plasma is produced is located in a distance of 500 μm, i.e., one diameter d_e behind the nozzle exit (see the typical plasma position indicated in **Figure 8**). Although the density is highest at the nozzle exit, the plasma should not be generated closer to the nozzle because of growing degradation effects. By employing different target species, various spectra can be obtained in the EUV and soft X-ray range. Noble gases with high atomic numbers such as xenon, argon, or krypton are broadband emitters, while oxygen or nitrogen each produces several narrow lines. The corresponding spectra can be found in **Figure 9**, produced by a system comparable to that described above and captured with a soft X-ray spectrometer, which is described in detail in [8]. Here, nitrogen is used in combination with a titanium filter,

http://dx.doi.org/10.5772/64149

resulting in a monochromatic emittance at λ = 2.88 nm in the water window, corresponding to the transition $1s^2 - 1S2p$ of the valence electron of the N^{5+} ion [40].

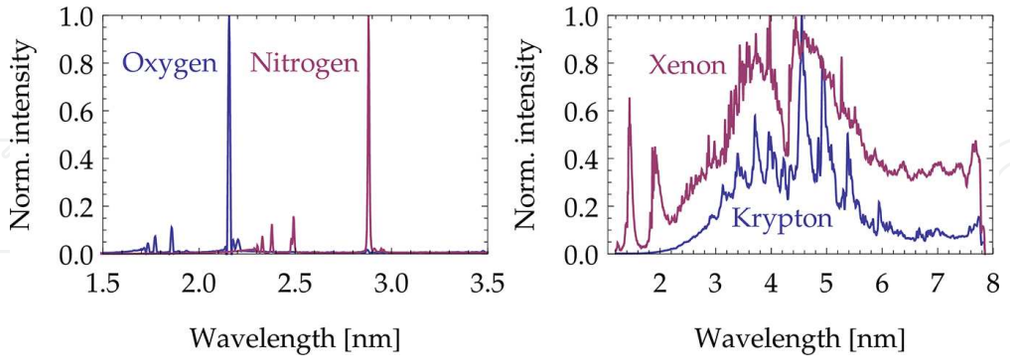

Figure 8. Photograph of experimental setup for plasma generation. The laser beam is focused by a lens into the vacuum chamber and generates the plasma right below the gas nozzle, which appears here in bluish color in the center of the chamber.

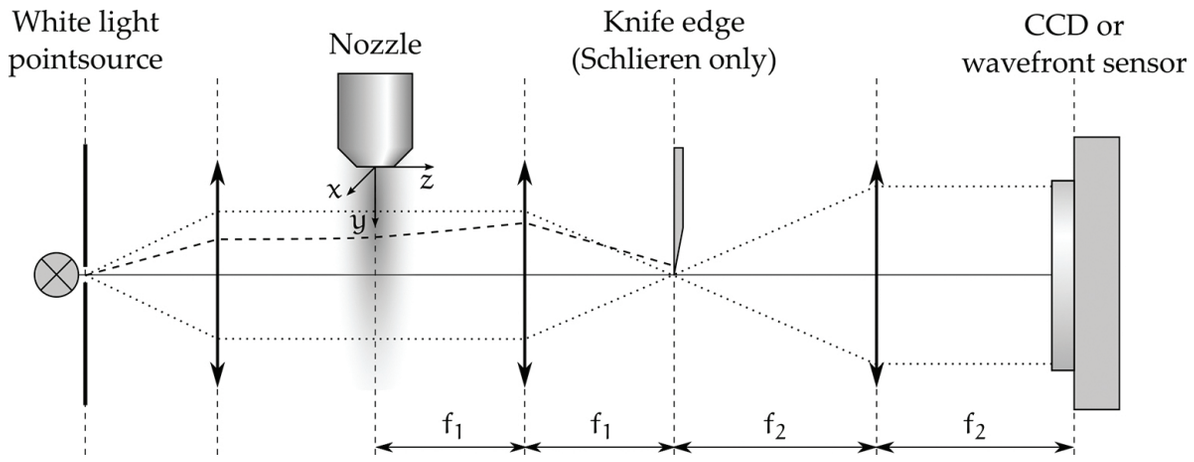

Figure 9. Principle of plasma generation employing jet targets: typically the plasma is generated close to the nozzle under vacuum conditions. Applying a background pressure p_b induces the barrel shock structure, which enhances plasma generation due to a local density increase.

In the approach pursued in this work, the background pressure p_b is increased to several tens of mbar in order to generate a barrel shock in the supersonic jet. For this purpose, helium is utilized as a background gas due to its high transmissivity of photons generated by the plasma. In addition, the optical path length of the resulting soft X-rays through helium is minimized by differential pumping. Another advantage of using helium as a surrounding gas is its large first ionization energy (24.6 eV) compared to that of nitrogen (14.5 eV) [41]. Thus, the critical power density to drive ionization by the incident laser beam is higher for helium, which ensures that only the target species nitrogen is ionized. Right behind the shock system generated in the jet, the particle density increases. In this manner, regions involving high densities of the target gas are obtained at comparably large distances from the nozzle. Thus,

the plasma can be generated further away from the nozzle exit, and degradation effects are minimized.

5. Gas jet and soft X-ray diagnostics

In order to characterize the supersonic gas jet and the evolving shock structure, two different methods are employed: the Schlieren technique for highly resolved qualitative imaging of density gradients and wavefront measurements with a Hartmann–Shack sensor in order to quantify the density distribution, but at a lower resolution. Both methods are described in detail in Sections 5.1 and 5.2.

The plasma is imaged by a pinhole camera and the number of the resulting soft X-ray photons is determined with a calibrated photodiode. A description of these tools follows in Section 5.3.

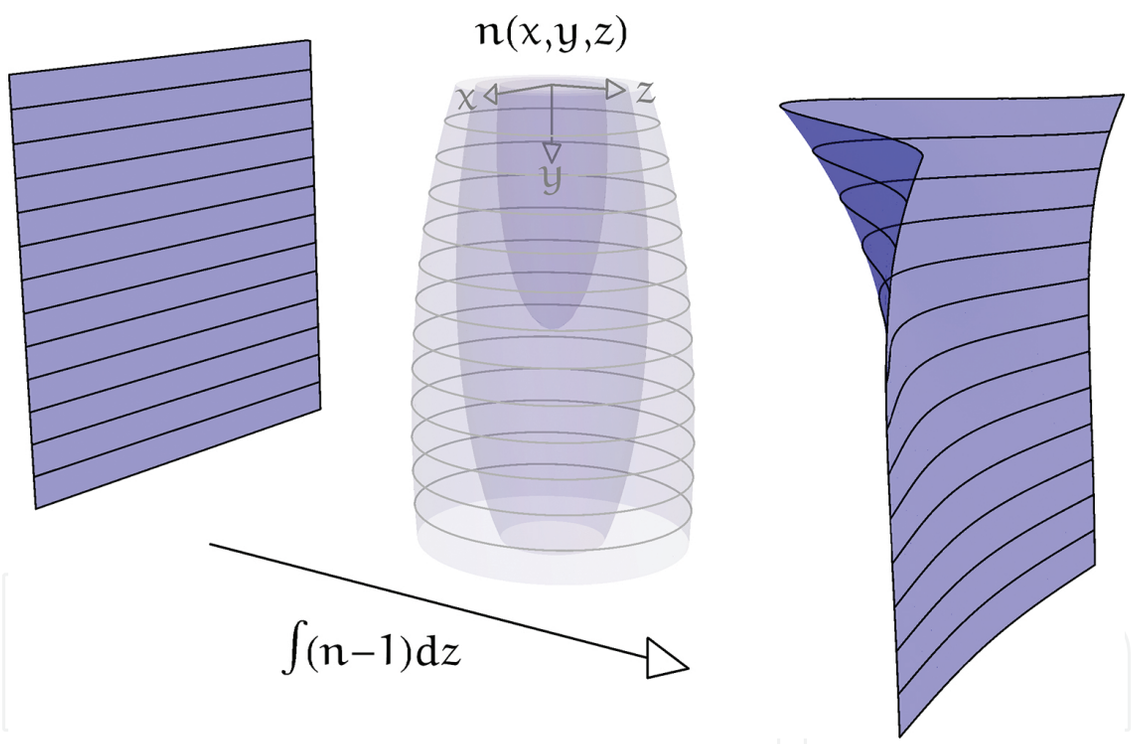

Figure 10. Characteristic emission spectra of various target gases, captured with a soft X-ray spectrometer.

5.1. Schlieren imaging

Schlieren imaging is a common technique in fluid dynamics that enables the qualitative measurement of density gradients [42]. The experimental setup is schematically shown in **Figure 10**. A pinhole with a diameter of 100 μm is illuminated by white light, and a focusing lens collimates the resulting beam, which then travels in the z-direction through the gas distribution of the jet target. The xy-plane at $z = 0$ is imaged by a 4f setup to a CCD camera

http://dx.doi.org/10.5772/64149

(Lumenera Lu160M) and captured with an exposure time of 50 μs. The camera is synchronized with the gas jet at a repetition rate of 10 Hz. Here, imaging lenses with focal lengths of f_1 = 160 mm and f_2 = 300 mm are used. A knife edge is moved close to the focal spot in between the two lenses, eliminating half of the spatial frequencies in the Fourier plane. The orientation of the blade determines which component of the density gradient will become visible. For example, as depicted in **Figure 10**, a knife edge aligned with the x-axis generates contrast proportional to the gradient of the refractive index $\partial n/\partial y$ corresponding to the density gradient $\partial \rho/\partial y$. Note, however, that in the Schlieren images shown below, the knife edge is aligned with the y-axis, so that density gradients within the jet are visualized in radial direction, thus emphasizing the barrel shock.

5.2. Wavefront monitoring

A Hartmann-Shack wavefront sensor [43, 44] is used to obtain quantitative information on the density distribution in the supersonic gas jet [34]. The experimental setup is mostly the same as that depicted in **Figure 10** for Schlieren imaging. However, the knife edge is removed and the CCD camera is replaced by the wavefront sensor. An initially plane wavefront of a test beam that travels through the target gas is deformed due to the spatial variation of the refractive index $n(x, y, z)$. The sensor splits the test beam into many subbeams by an array of microlenses, each producing a spot on a CCD camera (Lumenera Lu160M). The position of the spots contains the information of the local wavefront gradient. Thus, the deformation of the wavefront can be recovered. The spatial resolution Δx of a measured wavefront is equal to the pitch of the microlens array of 150 μm divided by the magnification factor f_2/f_1 = 1.88 of the 4f setup, yielding Δx = 80 μm.

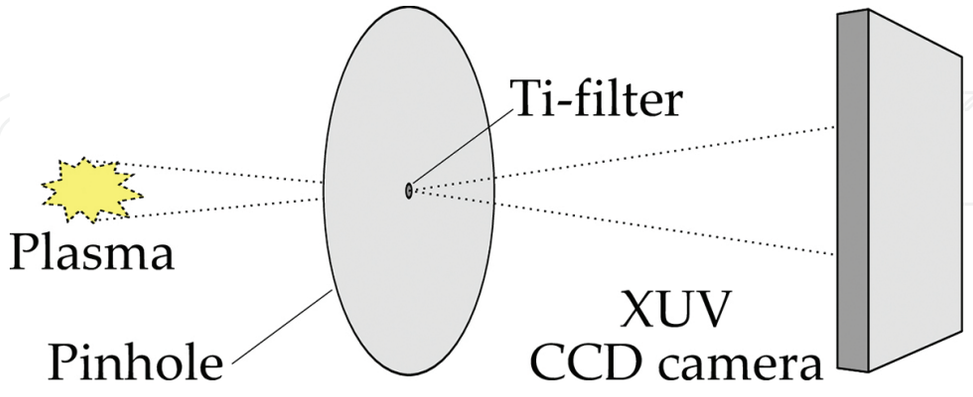

Figure 11. Experimental setup for Schlieren and wavefront measurements. The dotted lines represent the path of unrefracted light. The dashed line indicates a light ray that is refracted by varying distribution of gas density below the nozzle, thus hitting the knife edge and darkening the image. In order to monitor wavefront deformations, the CCD camera is replaced by a Hartmann–Shack sensor and the knife edge is removed.

The particle density distribution $N(x, y)$ in the nozzle plane $z = 0$ is recovered from a measured shape $w(x, y)$ of a deformed wavefront as follows. The test beam integrates $n(x, y, z)$ over the propagation direction z of the light beam, resulting in a difference $w(x, y)$ in the optical path, as illustrated in **Figure 11**. Now, it is assumed that in a plane corresponding to a constant $y = y_0$, $n(x, y_0, z)$ is approximated by a rotationally symmetric Gaussian shape with a maximum value $n_0(y_0) = n(0, y_0, 0)$. Then, the deformation of the wavefront reads

$$\begin{aligned} w(x,y) &= \int \left[n(x,y,z) - 1 \right] dz \\ &= \int \left[n_0(y) - 1 \right] \cdot \exp\left(-\frac{x^2}{2\sigma(y)^2} \right) \cdot \exp\left(-\frac{z^2}{2\sigma(y)^2} \right) dz \\ &= \left[n_0(y) - 1 \right] \cdot \sqrt{2\pi}\, \sigma(y) \cdot \exp\left(-\frac{x^2}{2\sigma(y)^2} \right). \end{aligned}$$

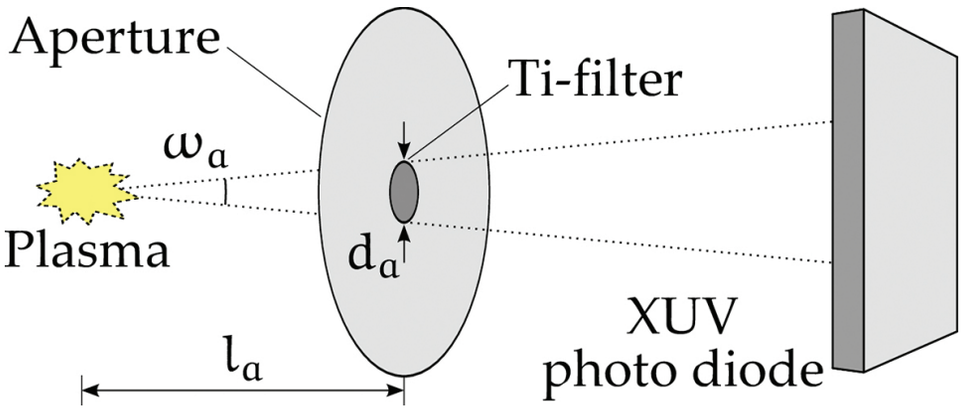

Figure 12. Wavefront deformation induced by the gas jet. The distribution of the optical density $n(x, y, z)$ increases the optical path length, resulting in the indicated wavefront deformation.

The standard deviation $\sigma(y)$ of $n(x, y, z)$ is determined from the shape of the measured deformation of the wavefront $w(x, y)$ by a Gaussian fit. The distribution of the refractive index in the plane $z = 0$ containing the jet axis is recovered by

$$n(x,y,0) - 1 = \frac{w(x,y)}{\sqrt{2\pi}\sigma(y)}. \tag{12}$$

Conversion of the refractive index $n(x, y, 0)$ into a particle density N is done by using the Lorentz-Lorenz formula [45]

$$\frac{n^2 - 1}{n^2 + 2} = \frac{4}{3}\pi\alpha N \tag{13}$$

http://dx.doi.org/10.5772/64149

where α, the polarizability of the considered gas particles, is derived using the values n = 1.0002974 and $N = 2.69 \times 10^{19}$ cm^{-3} for nitrogen under normal conditions [41] (at a temperature of 273.15 K and a pressure of 1013.25 mbar). In these calculations, the surrounding helium atmosphere is neglected because of its low refractive index that amounts to only a few percent as compared to that of the nitrogen jet.

5.3. Plasma characterization

Qualitatively, the plasma is characterized by a pinhole camera system as sketched in **Figure 12**. It consists of a phosphor-coated CCD camera (Lumenera Lu160M with three layers of phosphor P43 with a grain size of ≈ 1 μm) in combination with a titanium-filtered pinhole (100 μm diameter, Ti-layer 200 nm thick). This way, the intensity distribution of radiation at the wavelength λ = 2.88 nm is captured. Here, the luminescent area A is approximated by an ellipsoidal shape with the semiaxes a and b. Then, $A = \pi\, a\, b$, where a and b are defined as the full-widths at half-maximum of the intensity in the x- and y-directions. The uniformity of the plasma is characterized by its eccentricity $\varepsilon = \sqrt{a^2 - b^2}\,/\,a$. Examples of the intensity images are shown in **Figure 17** in combination with the corresponding Schlieren images of the gas jet for the case of both, gas issuing into vacuum and gas issuing into a background gas and thus forming a barrel shock.

Quantitatively, the peak brilliance Br of the plasma is derived by

$$Br = \frac{N_{ph}}{\tau\, \Omega A} \tag{14}$$

with the pulse duration τ, the solid angle Ω, and the source area A. The number of photons N_{ph} with a wavelength of λ = 2.88 nm is determined by a calibrated XUV photodiode (International Radiation Detectors, AXUV100), which is equipped with a titanium filter (thickness 200 nm, applied to a nickel mesh with a transmissivity of 0.89). As shown in **Figure 13**, only these photons reach the detector that propagate within a cone confined by a circular aperture with diameter d_a in a distance l_a to the plasma. Thus, the solid angle is defined by the corresponding opening angle $\omega_a = 2 \tan d_a/(2l_a)$ of the cone [46]

$$\Omega = 4\pi \sin^2 \sin^2 \frac{\omega_a}{4}. \tag{15}$$

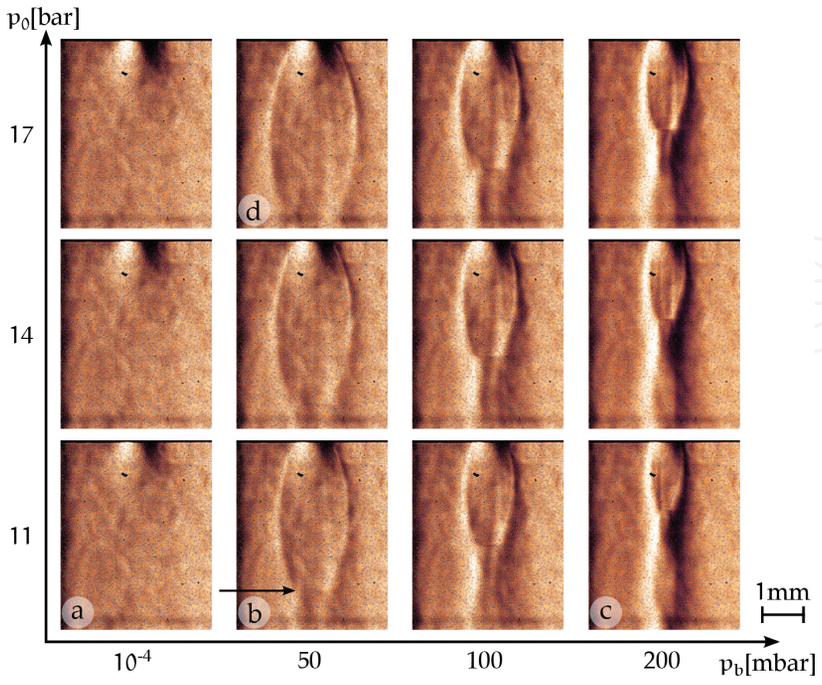

Figure 13. Principle of plasma characterization by pinhole camera.

In good approximation, the lifetime of the plasma is assumed to be $\tau = 6$ ns, which equals the duration of the exciting laser pulse. Finally, the luminescent area A is determined with a pinhole camera as described above.

6. Experimental results

First, the gas jet and the effect of a background pressure on the resulting flow structure are investigated using the techniques described in the previous section. The derived results are compared to theoretical relations discussed in Section 3. Subsequently, the effect of the barrel shock on the plasma generation is explored and the brilliance improvement of the soft X-ray source is quantified.

6.1. Characterization of the target gas jet

Depending on the stagnation and background pressure, the gas jet may form various shapes, which are discussed in the following. In previous studies of laser-produced soft X-ray sources, the nozzle was operated in the range $p_0 = 11–17$ bar at a background pressure of $p_b = 10^{-4}$ mbar, i.e., practically without any background gas. In this case, the emerging flow is in the scattering regime and does not show any discontinuities. Independently of p_0, the density distribution has a maximum value at the nozzle exit and rapidly falls off in all directions. The corresponding Schlieren images are taken with the knife edge aligned with the y-axis and can be found in **Figure 14** for the pressure range $p_0 = 11–17$ bar.

http://dx.doi.org/10.5772/64149

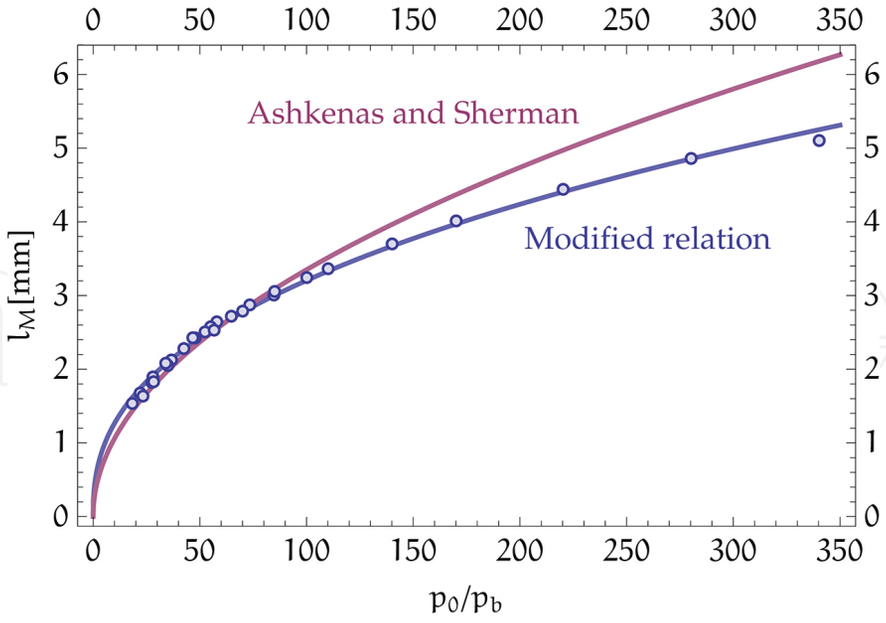

Figure 14. Principle of plasma characterization by diode measurement.

With rising background pressure, particle collisions increasingly affect the gas jet and retard its free expansion. At a certain distance from the nozzle, this results in a shock that is directly connected to a local decrease of the Mach number M. At the same time, the local particle density increases. This becomes evident in regions of the Schlieren images that show strong changes in intensity, implying high-density gradients. As can be seen, e.g., in **Figure 14(b)**, the shape of the resulting shock structure resembles a barrel, why it is referred to as a barrel shock. In the downstream direction, the barrel shock is terminated by the Mach disk, which is indicated in the Schlieren image by an arrow. In the present Schlieren pictures, the Mach disk is reproduced only weakly because the knife edge was aligned perpendicular to the disk and only density gradients parallel to the disk were detected.

Increasing p_b, as from **Figure 14(b)–(c)**, results in a confinement of the gas flow toward the nozzle axis—the lateral shocks approach each other and the Mach disk moves upstream. In contrast to this, increasing p_0 has the opposite effect, i.e., the radius of the barrel shock and the width σ of the density distribution increase and the Mach disk moves downstream, see **Figure 14(b)–(d)**. These two opposite effects allow generation of the same shock structure at different combinations of the pressures, provided that the ratio p_0/p_b stays constant.

From the Schlieren images as shown in **Figure 14**, the distance l_M between the Mach disk and the nozzle throat is derived for pressure ratios in the range $18 \le p_0/p_b \le 340$. In **Figure 15**, the resulting data set is compared to the empirical relation (11)

$$l_M = 0.67 \cdot d_e \left(\frac{p_0}{b_b} \right)^{1/2} \tag{16}$$

which has been derived by Ashkenas and Sherman [37] for a nondivergent nozzle. Apparently, the experimental results deviate from the depicted curve, especially for large pressure ratios. Most likely, this can be attributed to a different nozzle geometry as in the present situation. Here, a divergent orifice initially guides the supersonic expansion of the gas before it expands freely into the helium atmosphere. For that case, a relation of the form

$$l_M = d_e \left(\frac{p_0}{p_b} \right)^a \tag{17}$$

reveals good agreement with the measured shock distances as it is evident in **Figure 15**. By a least-squares fit routine, the exponent is derived to $a = 0.4034$.

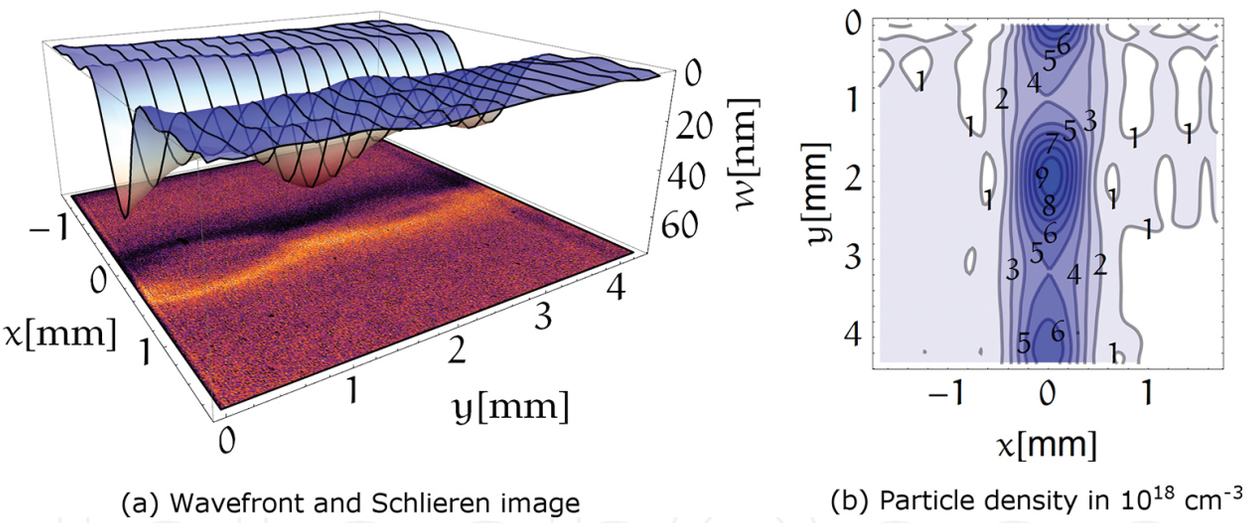

Figure 15. Schlieren images indicating the supersonic flow structure of an N_2 jet as a function of stagnation and background pressure (flow direction: top → bottom). (a) Scattering regime, no internal structures evolve; (b) continuum regime with barrel shock structure, the Mach disk is indicated by the arrow; (b) → (c) shock structure contracts for increasing background pressure; (b) → (d) shock structure inflates for increasing stagnation pressure.

In **Figure 16**, wavefront and Schlieren measurements are compared with each other for a stagnation pressure of $p_0 = 11$ bar and a background pressure of $p_b = 170$ mbar. The results of both techniques are well consistent. The particle density $N(x, y)$ shows the mean gas distribution inside the jet. In the downstream direction, along the nozzle axis, N first decreases to $N_{min} = 4.0 \times 10^{18}$ cm^{-3} and then increases again up to a maximum value of $N_{max} = 9.8 \times 10^{18}$ cm^{-3}. Subsequently, the wave-like behavior of the particle density is repeated at lower density values. The observed maxima coincide approximately with the positions where the lateral shocks interfere, forming a Mach disk.

http://dx.doi.org/10.5772/64149

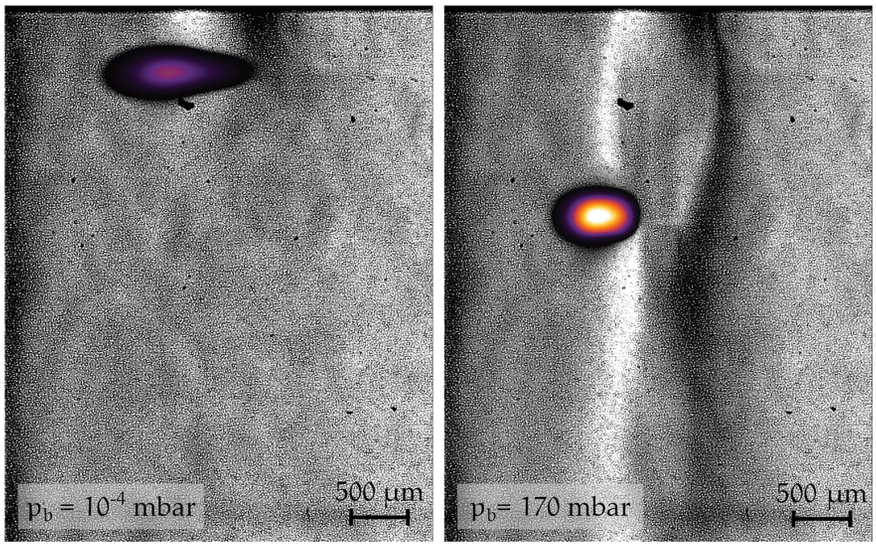

Figure 16. Distance between Mach disk and nozzle exit for various pressure ratios. The points are derived from the Schlieren images, the violet curve represents the empirical relation (11) from Ashkenas and Sherman [37] and the blue curve represents the modified relation given in Eq. (17) with $a = 0.4034$.

Employing the relations of gas dynamics introduced in Section 3, a rough theoretical estimate of the particle density ahead and behind the Mach disk is now compared to the results obtained with the wavefront sensor. Corresponding to the experimental situation, the density distribution along the symmetry axis of the gas jet is shown in terms of its stagnation value ρ_0 as shown in **Figure 6**. There, a normal shock induces a density increase from $\rho_{min} = 0.039\ \rho_0$ to $\rho_{max} = 0.170\ \rho_0$ in a distance of $l_M = 2.7$ mm to the nozzle throat. For the current pressure ratio of $p_0/p_b = 64.7$, this coincides with the position of the Mach disk.

In order to derive absolute density values, the stagnation density ρ_0 of the nitrogen jet is required. Following the ideal gas law, $p_0 = \rho_0\, R_{sp}\, T_0$ results in $\rho_0 = 12.65$ kg/m^3 with the specific gas constant for nitrogen $R_{sp,N_2} = 296.8$ J/(kg · K) [41], the temperature $T_0 = 293$ K, and pressure $p_0 = 11$ bar inside the vessel. Finally, particle densities ahead and behind the Mach disk are evaluated with the molecular mass of nitrogen $m_{N_2} = 4.653 \times 10^{-26}$ kg [41]. A comparison between the theoretical estimation and the measured values is given in **Table 1**.

	Theoretical estimate	**Measurement**
N_{min} (10^{18} cm^{-3})	10.6	4.0
N_{max} (10^{18} cm^{-3})	46.1	9.8

Table 1. Particle density ahead (N_{min}) and after (N_{max}) the barrel shock, given on the symmetry axis of the jet. Comparison between theoretical estimate and measurement.

The estimated values are of the same order of magnitude but larger than the experimental results. This discrepancy can be attributed to the spatial resolution of the wavefront sensor that is not able to resolve the high density value right behind a shock. Furthermore, the estimate

provides an upper limit of the particle density since in a simplification a conical source flow has been assumed. In fact, the stream lines of the flow are bended in lateral direction, stronger than the cone geometry presumes. Consequently, this results in a higher rarefaction of the gas and the typical bulbous barrel shock. This explains why values of the estimated particle densities, both of the maximum and the minimum, are higher than the corresponding measured values.

6.2. Characterization of the plasma enhancement

The effect of an increase in target gas density on the plasma generation is illustrated in **Figure 17** for a stagnation pressure of p_0 = 11 bar. Taking advantage of the barrel shock, obviously the brightness of the plasma is raised, whereas its size has decreased in the direction of the incident laser beam. Due to the increased target density, there are more emitters of soft X-ray radiation in the same volume. Besides, the absorption of laser energy is raised. Thus, the power density of the beam decreases more rapidly below its critical value and no further atoms are ionized. This confines the size of the plasma in the beam direction and explains its smaller size. Another mechanism causing the reduced size might be plasma defocusing [47]. Due to an increased plasma density, a stronger defocusing effect can be expected, limiting the ionization region. During the experiments, it turned out that generation of a plasma right below the Mach disk, where the density is expected to be at a maximum, is not the optimal position. It was found that even brighter and smaller plasmas occur when the laser is focused onto the edge of the jet at a location slightly above the Mach disk and after the barrel shock (see **Figure 17**). This behavior may be caused by reabsorption of soft X-rays by the surrounding nitrogen particles.

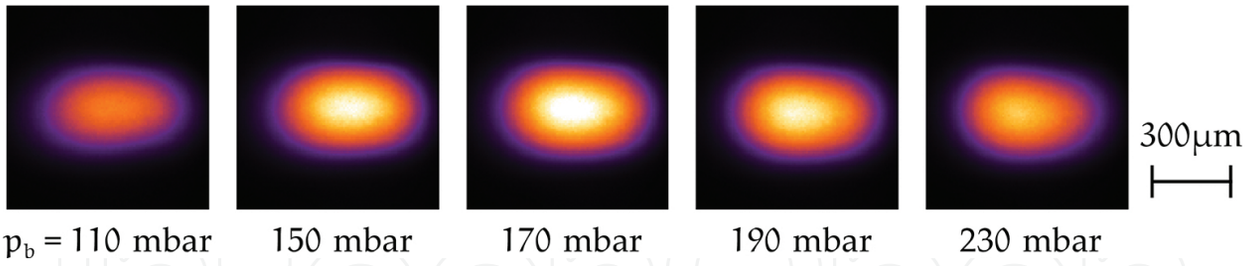

Figure 17. (a) Combination of quantitative wavefront and qualitative Schlieren image of the N_2 jet expanding from p_0 = 11 bar into an He atmosphere with p_b = 170 mbar. (b) Density distribution $N(x, y)$ of the N_2 jet in the plane z = 0, which results from the wavefront as described in Section 5.2.

The barrel shock is enclosed by a thin supersonic compressed layer, which becomes thicker at the Mach disk [36], leading to increased reabsorption. In order to study the brilliance improvement depending on the location of plasma generation with respect to shock structures in the jet, the latter were varied by changing the background pressure at a constant stagnation pressure (p_0 = 11 bar). By lowering p_b, the radius of the barrel shock is increased; conversely, with increasing p_b, the radius of the barrel shock decreases. Thus, with the location of the focus of the laser beam fixed, its relative location with respect to high-density regions behind the shock is changed. In **Figure 18**, intensity distributions of the plasma are shown for various

http://dx.doi.org/10.5772/64149

background pressures p_b. In this case, the location of plasma generation is kept constant. An optimum value is found at $p_b = 170$ (see also **Figure 17**).

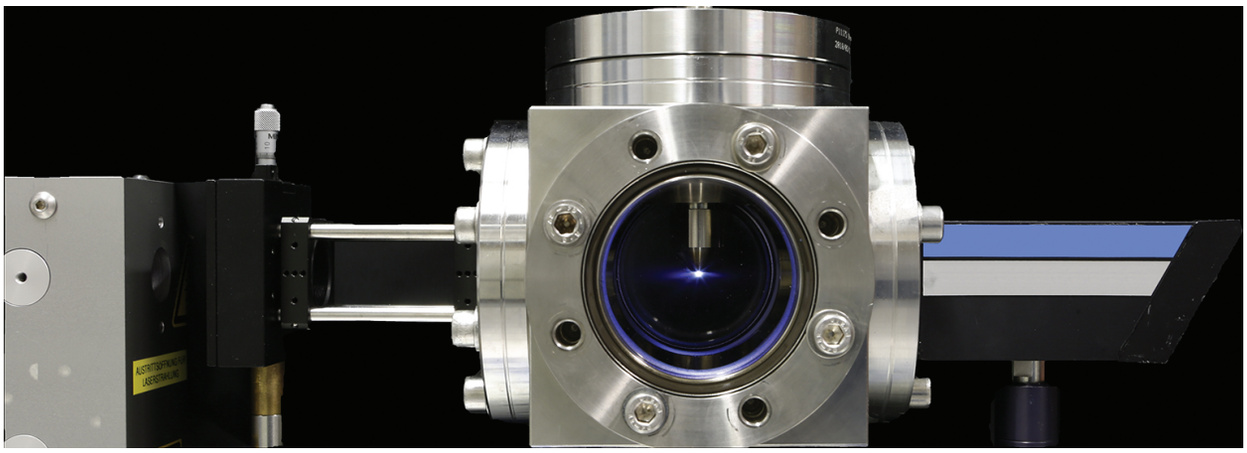

Figure 18. Pinhole camera images of the plasma superimposed on the Schlieren images of gas jet at $p_0 = 11$ bar. Left: under vacuum conditions $p_b = 10^{-4}$ mbar. Right: with ambient He atmosphere at $p_b = 170$ mbar. Both plasma images are an average of 30 single shots.

Unexpectedly, increasing both p_0 and p_b while preserving the pressure ratio p_0/p_b, does not lead to a considerable further increase in the brilliance of the source. Approaching high-pressure values ($p_0 = 17$ bar), quite the reverse happens: the plasma appears even darker. It can be assumed that, in fact, more soft X-ray photons are generated since the target density is increased. However, the density of the background gas is increased as well, which leads to higher reabsorption of the generated photons. The latter effect seems to dominate the former. It is expected that further efforts in differential pumping can shorten the path length of the soft X-rays through the outer helium gas so that the brilliance of the source can further be increased.

Now, parameters characterizing the plasma in the optimal case are compared with those of a plasma produced near the nozzle exit with a jet in the scattering regime. In both cases, the same stagnation pressure of $p_0 = 11$ bar is considered. Regarding the shape of the resulting plasma, which is represented by its luminescent area, it can be seen that the radiating area is reduced by a factor of 0.71 to $A = 0.063$ mm^2, and its eccentricity decreases slightly from $\varepsilon = 0.91$ to $\varepsilon = 0.80$ when a barrel shock is present. This results in a better brilliance and improves the coherence properties due to a smaller source size and a more uniform shape. The number of photons emitted per pulse and solid angle from the nitrogen plasma at a wavelength of $\lambda = 2.88$ nm is raised by a factor of 7.1 to a value of 1.2×10^{13} sr^{-1}. Based on these values, the peak brilliance can be computed. One finds an improvement by a factor of 10 to a value of $Br = 3.15 \times 10^{16}$ photons/(mm^2 mrad^2 s). This clearly demonstrates the advantage of utilizing the density increase across a barrel shock system. An overview of the characteristic parameters of the plasma is given in **Table 2**.

	Without barrel shock	With barrel shock	Factor
Radiating area (mm^2)	0.088	0.063	0.71
Eccentricity [1]	0.91	0.80	0.88
Photons/(solid angle · pulse) (sr^{-1})	1.66×10^{12}	1.18×10^{13}	7.10
Peak brilliance (mm^{-2} $mrad^{-2}$ s^{-1})	3.15×10^{15}	3.15×10^{16}	10.0

Table 2. Comparison of plasma emission characteristics at $\lambda = 2.88$ nm obtained with a nitrogen jet issuing into vacuum (no barrel shock) and into a background gas (with barrel shock).

7. Conclusion

Laser-produced plasmas based on gas targets serve as versatile and nearly debris-free soft X-ray sources at a table-top size. In this chapter, a method has been shown by which the brilliance of gas targets can be improved. To this end, a background pressure is applied to the gas jet that leads to a strong recompression of the target particles. For the example of an underexpanded supersonic nitrogen jet, the resulting barrel shock has been qualitatively visualized by the Schlieren photography. The corresponding density distribution was obtained by a quantitative Hartmann-Shack measurement. Measured values of the shock location and particle densities are of the same order of magnitude as those of a first estimate that was partly based on correlations. The size of the resulting plasma is reduced by a factor of 0.71 and its shape becomes more uniform, thus improving the coherence properties of the source. At the same time, the number of photons per solid angle at $\lambda = 2.88$ nm is raised by a factor of 7.1. In this manner, the brilliance of the source is increased by a factor of 10.0 to $Br = 3.15 \times 10^{16}$ photons/(mm^2 $mrad^2$ s). Even greater increases may be obtained by using hydrogen as the background gas since H_2 shows a 13 times lower absorption of the generated X-rays compared to He [48]. However, for safety reasons H_2 has not been employed here. A further increase in the plasma's brilliance is to be expected with increasing the stagnation and background pressure. An essential condition for achieving this is an improvement in the differential pumping system in order to lower the reabsorption of the soft X-rays by the background gas.

Acknowledgements

The author kindly acknowledges support by Deutsche Forschungsgemeinschaft within Sonderforschungsbereich 755 "Nanoscale photonic imaging." Furthermore, the author acknowledges the permission to reproduce material [25], which has been previously published by IOP Publishing & Deutsche Physikalische Gesellschaft under CC BY-NC-SA license.

Author details

Tobias Mey

Address all correspondence to: tobias.mey@llg-ev.de

Laser-Laboratorium Göttingen e.V., Göttingen, Germany

References

[1] Attwood D. Soft X-Rays and Extreme Ultraviolet Radiation. Cambridge: Cambridge University Press; 1999.

[2] Bakshi V, editor. EUV Lithography. SPIE Press; Bellingham, Washington, USA. 2008. 702 pp.

[3] Wu B, Kumar A. Extreme ultraviolet lithography: a review. Journal of Vacuum Science & Technology B. 2007; 25: 1743–1761. DOI: 10.1116/1.2794048

[4] Scholze F et al. New PTB beamlines for high-accuracy EUV reflectometry at BESSY II. Soft X-Ray and EUV Imaging Systems. .Proc. SPIE 4146. 2000; 72. DOI: 10.1117/12.406678

[5] Scholze F, Laubis C. Use of EUV scatterometry for the characterization of line profiles and line roughness on photomasks. In: Mask and Lithography Conference (EMLC), 24th European Conference; 2008.

[6] Banyay M, Juschkin L. Table-top reflectometer in the extreme ultraviolet for surface sensitive analysis. Applied Physics Letters. 2009; 94(6): 063507. DOI: 10.1063/1.3079394

[7] Chen JG. NEXAFS investigations of transition metal oxides, nitrides, carbides, sulfides and other interstitial compounds. Surface Science Reports. 1997; 30: 1–152. DOI: 10.1016/s0167-5729(97)00011-3

[8] Peth C, Barkusky F, Mann K. Near-edge X-ray absorption fine structure measurements using a laboratory-scale XUV source. Journal of Physics D. 2008; 41: 105202. DOI: 10.1088/0022-3727/41/10/105202

[9] Stöhr J. NEXAFS Spectroscopy (Springer Series in Surface Sciences). Springer; Berlin Heidelberg, Germany. 2003.

[10] Da Silva LB et al. X-ray laser microscopy of rat sperm nuclei. Science. 1992; 258: 269–271. DOI: 10.1126/science.1411525

[11] Berglund M et al. Compact water-window transmission X-ray microscopy. Journal of Microscopy. 2000; 197: 268–273. DOI: 10.1046/j.1365-2818.2000.00675.x

[12] Hertz HM et al. Laboratory X-ray microscopy for high-resolution imaging of environmental colloid structure. Chemical Geology. 2012; 329: 26–31. DOI: 10.1016/j.chemgeo.2011.07.012

[13] Barkusky F et al. Direct photoetching of polymers using radiation of high energy density from a table-top extreme ultraviolet plasma source. Journal of Applied Physics. 2009; 105: 014906. DOI: 10.1063/1.3054565

[14] Haney SJ et al. Prototype high-speed tape target transport for a laser plasma soft-x-ray projection lithography source. Applied Optics. 1993; 32: 6934–6937. DOI: 10.1364/ao.32.006934

[15] Wagner C, Harned N. EUV lithography: lithography gets extreme. Nature Photonics. 2010; 4: 24–26. DOI: 10.1038/nphoton.2009.251

[16] Peth C et al. XUV laser-plasma source based on solid Ar filament. Review of Scientific Instruments. 2007; 78: 103509. DOI: 10.1063/1.2801882

[17] Hansson BAM. Characterization of a liquid-xenon-jet laser-plasma extreme-ultraviolet source. Review of Scientific Instruments. 2004; 75: 2122–-2129. DOI: 10.1063/1.1755441

[18] Vogt U et al. High-resolution spatial characterization of laser produced plasmas at soft x-ray wavelengths. Applied Physics B. 2004; 78: 53–58. DOI: 10.1007/s00340-003-1338-9

[19] Jansson PAC et al. Liquid-tin-jet laser-plasma extreme ultraviolet generation. Applied Physics Letters. 2004; 84: 2256–2258. DOI: 10.1063/1.1690874

[20] Richardson M et al. High conversion efficiency mass-limited Sn-based laser plasma source for extreme ultraviolet lithography. Journal of Vacuum Science & Technology B. 2004; 22: 785–790. DOI: 10.1116/1.1667511

[21] Wieland M et al. EUV and fast ion emission from cryogenic liquid jet target laser-generated plasma. Applied Physics B. 2001; 72: 591–597. DOI: 10.1007/s003400100542

[22] Bakshi V, editor. EUV Sources for Lithography. SPIE Press; Bellingham, Washington, USA. 2006.

[23] Rymell L, Hertz HM. Debris elimination in a droplet-target laser-plasma soft x-ray source. Review of Scientific Instruments. 1995; 66: 4916–4920. DOI: 10.1063/1.1146174

[24] Rakowski R et al. Characterization and optimization of the laser-produced plasma EUV source at 13.5 nm based on a double-stream Xe/He gas puff target. Applied Physics B. 2010; 101: 773–789. DOI: 10.1007/s00340-010-4327-9

[25] Mey T et al. Brilliance improvement of laser-produced soft x-ray plasma by a barrel shock. New Journal of Physics. 2012; 14: 073045. DOI: 10.1088/1367-2630/14/7/073045

[26] Fiedorowicz H et al. Compact laser plasma EUV source based on a gas puff target for metrology applications. Journal of Alloys and Compounds. 2005; 401: 99–103. DOI: 10.1016/j.jallcom.2005.02.069

[27] Morgan CG. Laser-induced breakdown of gases. Reports on Progress in Physics. 1975; 38: 621–665. DOI: 10.1088/0034-4885/38/5/002

[28] Fiedorowicz H et al. Investigation of soft X-ray emission from a gas puff target irradiated with a Nd:YAG laser. Optics Communications. 1999; 163: 103–-114. DOI: 10.1016/s0030-4018(99)00100-5

[29] Müller M et al. Emission properties of ns and ps laser-induced soft X-ray sources using pulsed gas jets. Optics Express. 2013; 21: 12831. DOI: 10.1364/oe.21.012831

[30] Mayer-Kuckuk T. Atomphysik. Teubner Verlag; Stuttgart, Germany. 1997.

[31] Komori H et al. EUV radiation characteristics of a CO_2 laser produced Xe plasma. Applied Physics B. 2006; 83: 213–218. DOI: 10.1007/s00340-006-2172-7

[32] Wieghardt K. Theoretische Strömungslehre. Universitätsverlag; Göttingen, Germany 2005.

[33] Spurk J, Aksel N. Strömungslehre. Berlin: Springer; 2010.

[34] Peth C et al. Characterization of gas targets for laser produced extreme ultraviolet plasmas with a Hartmann-Shack sensor. Review of Scientific Instruments. 2004; 75: 3288–3293. DOI: 10.1063/1.1791314

[35] Muntz EP et al. Some characteristics of exhaust plume rarefaction. AIAA Journal. 1970; 8: 1651–1658. DOI: 10.2514/3.49856

[36] Rebrov AK. Free jets in vacuum technologies. Journal of Vacuum Science & Technology A. 2001; 19: 1679–1987. DOI: 10.1116/1.1382649

[37] Ashkenas H, Sherman FS. The structure and utilization of supersonic free jets in low density wind tunnels. In: Proceedings of the Fourth Symposium on Rarefied Gas Dynamics; 1966. pp. 84–105.

[38] Proch D, Trickl T. A high-intensity multi-purpose piezoelectric pulsed molecular beam source. Review of Scientific Instruments. 1989; 60: 713. DOI: 10.1063/1.1141006

[39] Phuoc TX. Laser spark ignition: experimental determination of laser-induced breakdown thresholds of combustion gases. Optics Communications. 2000; 175: 419–423. DOI: 10.1016/s0030-4018(00)00488-0

[40] Moore CE. Selected tables of atomic spectra, atomic energy levels and multiplet tables — N IV, N V, N VI, N VII. National Standard Reference Data Series, NSRDS-NBS3 (Sect. 4). Washington, D.C. 1971.

[41] Haynes WM, editor. CRC Handbook of Chemistry and Physics, 94th ed. CRC Press; Boca Raton, Florida 2013.

[42] Settles G. Schlieren & Shadowgraph Techniques. Springer; Berlin Heidelberg, Germany 2006.

[43] Hartmann J. Bemerkungen über den Bau und die Justierung von Spektrographen. Zeitschrift für Instrumentenkunde. 1900; 20: 47.

[44] Platt BC, Shack R. History and principles of Shack-Hartmann wavefront sensing. Journal of Refractive Surgery. 2001; 17: 573–577.

[45] Born M, Wolf E. Principles of Optics: Electromagnetic Theory of Propagation, Interference and Diffraction of Light. Cambridge University Press; Cambridge, UK. 1999.

[46] Bronstein IN et al. Taschenbuch der Mathematik. Europa-Lehrmittel; Haan-Gruiten, Germany.2013.

[47] Auguste T et al. Defocusing effects of a picosecond terawatt laser pulse in an underdense plasma. Optics Communications. 1992; 89: 145–148. DOI: 10.1016/0030-4018(92)90148-k

[48] Henke BL et al. X-ray interactions: photoabsorption, scattering, transmission, and reflection at E = 50-30,000 eV, Z = 1-92. Atomic Data and Nuclear Data Tables 1993; 54: 181–342. DOI: 10.1006/adnd.1993.1013